EDGE ARTICLE

Check for updates

Constructing a photoferroelectric semiconductor by regulating non-covalent interactions through halogen substitution

Yueyue He, [a] Shufang Wu, [a] Xiaofei Li, [a] Qi Wang, [a] Ruifang Zhao, [a] Lin Pan, [a] Chengbing Qin, [bd] Xian-Ming Zhang*[c] and Dongying Fu [*ab]

The advantages of molecular ferroelectrics lie in the "designability" and "multifunctionality", and the molecular-level regulation ability has opened up a brand-new dimension for ferroelectric materials. Non-covalent interactions play a crucial role in the construction of molecular ferroelectrics. However, there remain significant challenges in balancing the strength and reversibility of non-covalent interactions, as well as achieving long-range ordered arrangements. Therefore, a systematic study of non-covalent interactions in the structure is the key to construct high-performance molecular ferroelectrics. Here, we introduced halogenated amines with large dipole moments into adjacent inorganic layers to regulate the non-covalent interactions in the structure, thereby inducing the generation of ferroelectricity. Through a halogen substitution strategy to introduce chlorine (Cl) atoms on PA^+ (n-propylaminium) cations, hybrid perovskite photoferroelectric semiconductor $(Cl-PA)_2PbBr_4$ (Cl-PA$^+$ is 3-chloropropylaminium) with large piezoelectric response ($d_{33} = 36$ pC/N) and high Curie temperature ($T_c = 365$ K) was obtained. Compared with non-ferroelectric $(PA)_2PbBr_4$ ($\mu_{PA} = 1.2$ D), the larger dipole moment ($\mu_{Cl-PA} = 3.3$ D) and the directional ordered arrangement of Cl-PA$^+$ in $(Cl-PA)_2PbBr_4$ synergistically induce its ferroelectricity. More importantly, when Cl replaces H, it affects the hydrogen bond network between the organic cation and the inorganic layer, enhancing the dynamic freedom of the Cl-PA$^+$ cations, making the structure of $(Cl-PA)_2PbBr_4$ more prone to phase transitions when the temperature changes. The hydrogen bonding and halogen–halogen interactions in $(Cl-PA)_2PbBr_4$ lead to the directional and ordered arrangement of Cl-PA$^+$ cations, breaking the centrosymmetric structure and synergistically promoting the generation of ferroelectricity. This work has confirmed the significance of non-covalent interactions in the construction of ferroelectrics.

Introduction

Molecular ferroelectrics are typically composed of organic or organic–inorganic hybrid materials, which may be lighter, more flexible, and easier to process compared to traditional inorganic ferroelectrics.[1–4] Although under the guidance of "Ferroelectrochemistry" theory, many high-performance molecular ferroelectrics have been designed, synthesized and applied.[5] However, there have always been significant challenges in accurately constructing molecular ferroelectrics. Taking perovskite-type molecular ferroelectrics as an example, the matching of organic and inorganic parts, as well as how to induce non-centrosymmetric crystal structures, should be considered in the design.[6–10] Symmetry breaking is a necessary condition, which requires that the crystal structure of ferroelectrics must belong to one of the 10 polarity point groups.[11] Generally speaking, chiral centers can be introduced to forcibly break symmetry, and molecular arrangement can also be regulated through hydrogen bonding, van der Waals forces (VDW), or π–π stacking.[5,12] Non-covalent interactions (such as hydrogen bonds, VDW interactions, π–π stacking, halogen bonds, *etc.*) are mostly present in such materials and are of great significance for maintaining the order of the crystal structure and the mechanism of polarization reversal, which enable molecules to self-assemble into ordered structures under mild conditions, facilitating the regulation of ferroelectric properties through molecular design.[2,13] Firstly, non-covalent interactions have moderate strength and dynamic reversibility, which allow molecular units to undergo rearrangement under an external electric field, thereby achieving polarization direction reversal. Secondly, the weak bond properties of non-covalent

a Institute of Crystalline Materials, Shanxi University, Taiyuan, Shanxi 030006, P. R. China. E-mail: dyfu@sxu.edu.cn

b State Key Laboratory of Quantum Optics Technologies and Devices, Shanxi University, Taiyuan, Shanxi 030006, P. R. China

c College of Chemistry, Key Laboratory of Interface Science and Engineering in Advanced Material, Ministry of Education, Taiyuan University of Technology, Taiyuan, Shanxi 030024, P. R. China

d Institute of Laser Spectroscopy, Collaborative Innovation Center of Extreme Optics, Shanxi University, Taiyuan, Shanxi 030006, P. R. China

interactions enable the material to switch between different phase states, providing a driving force for ferroelectric behavior. In short, non-covalent interactions play a crucial role in achieving efficient ferroelectricity by dynamically regulating molecular arrangement, stabilizing polar structures, driving phase transitions, and reducing the energy barrier for polarization flipping. For example, the ferroelectric phase transition of classic ferroelectric KH_2PO_4 (potassium dihydrogen phosphate) is related to the ordered–disordered motion of hydrogen bond protons, and hydrogen bonds play a crucial role in the generation of its ferroelectricity.[14] The high polarization intensity in diisopropylammonium bromide (DIPAB) is due to the forced dipole alignment of hydrogen bonds, and the phase transition process is accompanied by dynamic recombination of hydrogen bonds.[2] In addition, the coercive field of metal-free perovskite ferroelectrics MDABCO–NH_4–$(PF_6)_3$ and MDABCO–NH_4–I_3 (MDABCO = N-methyl-N'-diazabicyclo [2.2.2] octonium) is regulated by hydrogen bonding, with a modulation amplitude of up to 10 times.[15]

Although we are aware of the significance of non-covalent interactions in the construction of molecular ferroelectrics, research in this area is still very scarce. In particular, further research is needed to design high-performance molecular ferroelectrics by utilizing the synergistic effects of multiple non-covalent interactions. Constructing molecular ferroelectrics by leveraging the synergistic effect of non-covalent interactions involves integrating multiple weak interactions to achieve precise control of molecular arrangement, enhancement of polarization, and optimization of dynamic response performance.[16,17] The synergistic effect of non-covalent interactions essentially lies in the molecular engineering of "combining rigidity and flexibility", which can lock the molecular polarity arrangement through highly directional forces (hydrogen bonds or halogen bonds), leading to symmetry breaking.[18–21] Meanwhile, the weak interaction of the flexible chain as a dynamic response unit provides a low-energy barrier flipping path, endowing the material with reversibility. However, the main challenge lies in how to balance the intensities and directions of various interactions, and avoid instability of the structure due to mutual competition.[22] We can take advantage of the designability of molecular ferroelectrics to modify organic amine units at the molecular level and construct multiple non-covalent interactions that work collaboratively in the system. The in-depth analysis of the selective regulation of non-covalent interactions and the structure–activity relationship is beneficial for us to accurately construct multifunctional molecular ferroelectrics.

Herein, we regulated the non-covalent interactions in the structure by modifying the organic components. Starting from non-ferroelectric $(PA)_2PbBr_4$ (PA^+ is n-propylaminium), we introduced halogenated amines $Cl-PA^+$ ($Cl-PA^+$ is 3-chloropropylaminium) with large dipole moments into adjacent inorganic layers to regulate non-covalent interactions in the structure, thereby inducing ferroelectricity in $(Cl-PA)_2PbBr_4$. After replacing the H atom in the PA^+ with a Cl atom, the dynamic response ability of the $Cl-PA^+$ cation and the lattice strain of the inorganic framework were significantly enhanced by increasing the molecular polarity and reconstructing the hydrogen bond network. Under the synergistic effect of hydrogen bonding and halogen–halogen interaction, $Cl-PA^+$ cations undergo directional ordered rearrangement, resulting in symmetry breaking in the structure of $(Cl-PA)_2PbBr_4$. The weakening of hydrogen bonds between the inorganic and organic parts from $(PA)_2PbBr_4$ to $(Cl-PA)_2PbBr_4$ gave $Cl-PA^+$ cations a higher degree of freedom, and the ferroelectricity in $(Cl-PA)_2PbBr_4$ relies on the synergistic effect between hydrogen bonds and halogen–halogen interactions. This result confirms that non-covalent interactions can not only adjust the molecular arrangement and promote symmetry breaking in the construction of molecular ferroelectrics, but also regulate the ordered-disordered transition of interlayer organic units, thereby triggering ferroelectric phase transition. Furthermore, possibly due to the existence of halogen–halogen interactions, $(Cl-PA)_2PbBr_4$ exhibits significantly better piezoelectric properties than other similar molecular ferroelectrics, with its d_{33} coefficient reaching up to 36 pC/N.

Results and discussion

As shown in Scheme 1, when a Cl atom replaces a certain H atom in the PA^+ cation, it will change the dipole moment and volume of the cation, which will inevitably affect the arrangement and rotational freedom of the cation in the inorganic layer. The ordered arrangement and dynamic movement ability of interlayer organic units are the "switch" and "regulator" for the two-dimensional (2D) molecular ferroelectrics.[23–25] From a structural perspective, molecules with large dipole moments are arranged in the crystals, and the inherent dipole directions tend towards a synergistic orientation, which can easily break the symmetry of the crystal and induce spontaneous polarization.[26] Meanwhile, the configuration and movement of cations also have a significant impact on the lattice distortion of the inorganic framework, resulting in the coupling of dipole-lattice distortion to achieve macroscopic polarization reversal.[27] Essentially, the dipole ordered arrangement of organic amines and the distortion of inorganic frameworks are both achieved through non-covalent interactions. Therefore, the dipole moment of organic amines often synergizes with the distortion of inorganic frameworks, and this synergistic mechanism is crucial in the design of molecular ferroelectrics. In $(Cl-PA)_2$-$PbBr_4$, the octahedral tilt of the inorganic layer and the dipole orientation of the $Cl-PA^+$ cations jointly determine the overall polarization direction of the system.

The stochiometric ratio 2 : 1 of the $Cl-PA^+$ cations and $Pb(CH_3COO)_2 \cdot 3H_2O$ was used to synthesize $(Cl-PA)_2PbBr_4$ in the refrigerator with HBr solution (48%) (Experimental section), and the structure of $(PA)_2PbBr_4$ has been reported in previous literature.[28] Fig. 1 is the structure of $(PA)_2PbBr_4$ and $(Cl-PA)_2$-$PbBr_4$ at room temperature. The crystal structures of $(PA)_2PbBr_4$ and $(Cl-PA)_2PbBr_4$ are composed of infinite layers of corner-sharing $PbBr_6$ octahedra, which are separated by bilayers of the organic cations PA^+ and $Cl-PA^+$, respectively. This arrangement forms a typical 2D monolayer Ruddlesden–Popper organic–inorganic hybrid perovskite structure.[29] However, there is
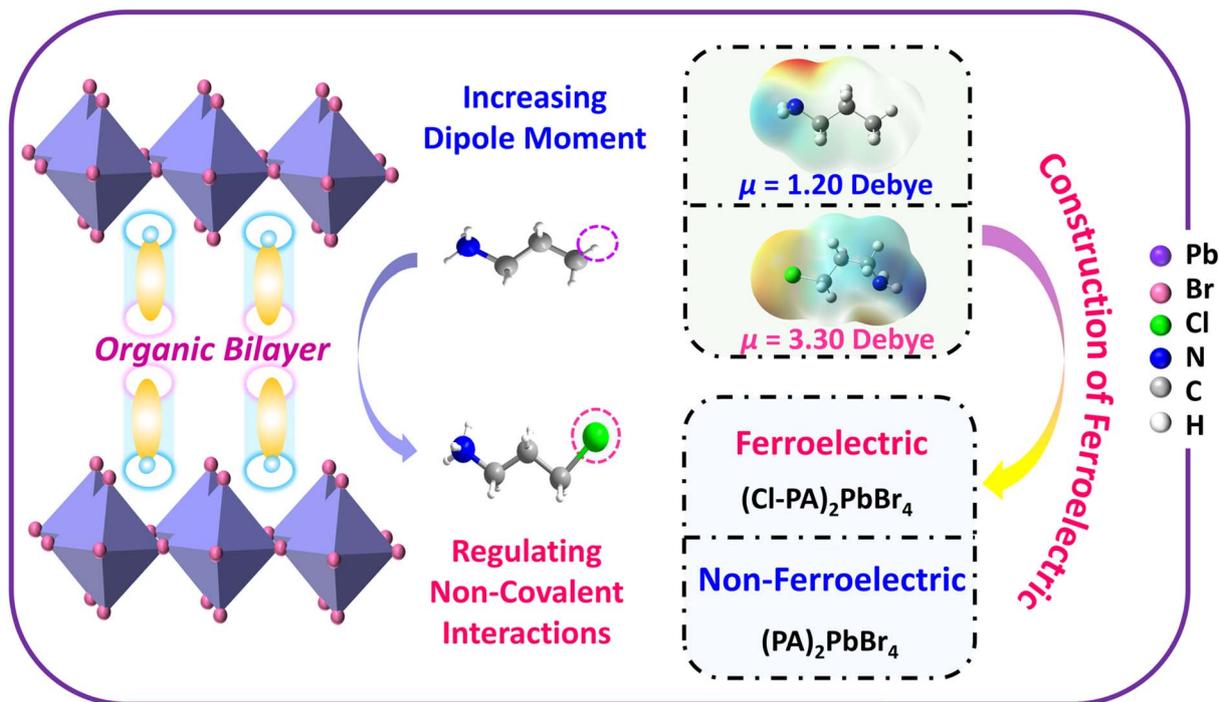
Scheme 1 Regulating non-covalent interactions to construct a photoferroelectric semiconductor.

a significant difference in the arrangement of PA$^+$ cations and Cl-PA$^+$ cations between adjacent inorganic layers in the two compounds. In (PA)$_2$PbBr$_4$ (Fig. 1a), the dipole direction of each PA$^+$ cation will exhibit a reverse dipole at the corresponding position of the symmetry center, resulting in a vector sum of zero. The dipole of PA$^+$ cations in one layer is upward, while that of the other layer at the symmetrical position is downward, resulting in the overall net dipole being zero. Meanwhile, the octahedra may also be arranged in an anti-parallel inclined or rotational symmetrical manner, such that the local dipole of each octahedron is counterbalanced by the opposite dipole of the adjacent octahedron. The dipole moment vector of organic cations in the structure and the net dipole moment of the entire inorganic skeleton are both zero. Therefore, in both the organic and inorganic parts, the dipole moments cancel each other out at the microscopic level. Fig. 1a shows that (PA)$_2$PbBr$_4$

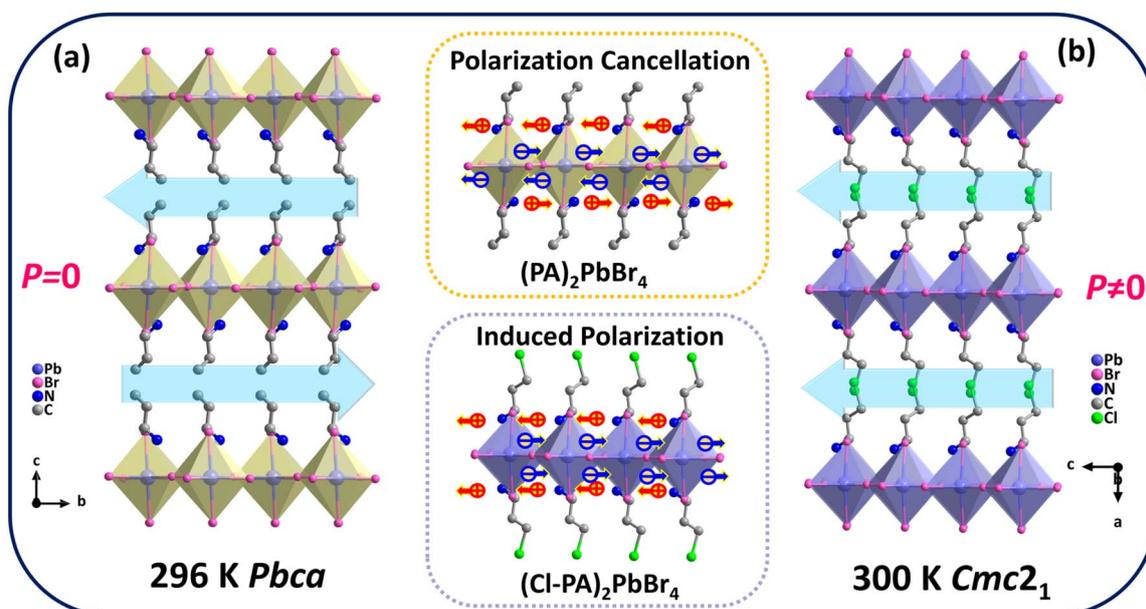**Fig. 1** The crystal structures of (PA)$_2$PbBr$_4$ (a) and (Cl-PA)$_2$PbBr$_4$ (b) at room temperature.

crystallizes in the centrosymmetric *Pbca* space group (point group *mmm*) at 296 K. In contrast to $(PA)_2PbBr_4$, $(Cl-PA)_2PbBr_4$ has an asymmetric dipole arrangement in the structure. The polarization generated by the inorganic skeleton and the polarization generated by all organic cations will not cancel each other, resulting in a large net spontaneous polarization (P_s) at the macroscopic level. At 300 K, $(Cl-PA)_2$-$PbBr_4$ crystallized in the non-centrosymmetric polarity $Cmc2_1$ space group (point group *mm*2) (Fig. 1b). The generation of net dipole in $(Cl-PA)_2$-$PbBr_4$ is achieved through the oriented and ordered arrangement of the $Cl-PA^+$ organic layer and structural distortion of the inorganic layer. Fundamentally, the reason for the structural differences between the two compounds is the substitution of the H atom on PA^+ cations by the Cl atom, which affects the non-covalent interactions in the structure. Regarding the analysis of how interlayer molecular modification can regulate non-covalent interactions within the structure to induce ferroelectricity, we will provide a detailed discussion in the following sections.

In addition to constructing polar structures, structural phase transitions serve as a key mechanism for triggering symmetry breaking, thereby inducing the generation of spontaneous polarization.[5] Before testing the phase transition of $(PA)_2PbBr_4$ and $(Cl-PA)_2PbBr_4$, we verified the phase purity of the two compounds through powder X-ray diffraction (PXRD). The experimental PXRD results of $(Cl-PA)_2PbBr_4$ and $(PA)_2PbBr_4$ are in agreement with the simulated patterns, indicating its good crystallinity and high phase purity (Fig. S1a and b). We also noticed that the change of interlayer cations from PA^+ to $Cl-PA^+$ had little effect on the PXRD diffraction peaks of the compounds. This smaller difference is mainly due to larger $Cl-PA^+$ cations occupying more space, which increases the inter-layer spacing between inorganic layers and causes the corresponding diffraction peaks to shift towards lower 2θ angles (Fig. S1c). Differential scanning calorimetry (DSC) tests were employed to investigate the phase transition behavior of $(PA)_2$-$PbBr_4$ and $(Cl-PA)_2PbBr_4$. The DSC thermogram revealed two pairs of reversible peaks during both heating and cooling processes, indicating two reversible phase transitions at temperatures of 348/341 K and 365/357 K in $(Cl-PA)_2PbBr_4$ (Fig. 2a). In contrast, there was no phase transition observed in $(PA)_2PbBr_4$ with temperature changes (Fig. S2). Subsequently,
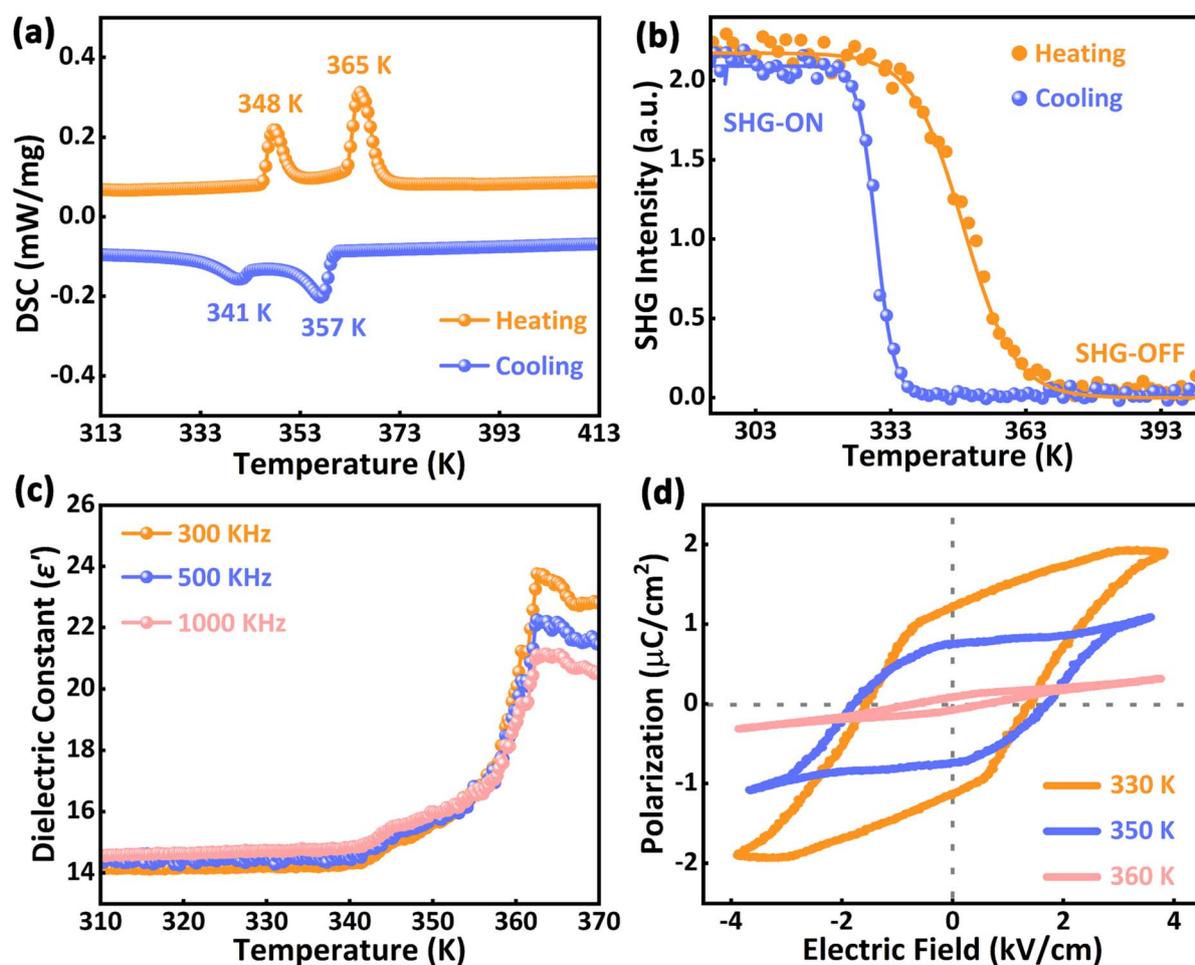

Fig. 2 Characterization of ferroelectricity of $(Cl-PA)_2PbBr_4$. (a) The phase transition behavior of $(Cl-PA)_2PbBr_4$. (b) The changes in SHG signals during the heating and cooling processes. (c) Variable-temperature dielectric measurements of $(Cl-PA)_2PbBr_4$. (d) Temperature-dependent variation of the P–E hysteresis loops of $(Cl-PA)_2PbBr_4$.
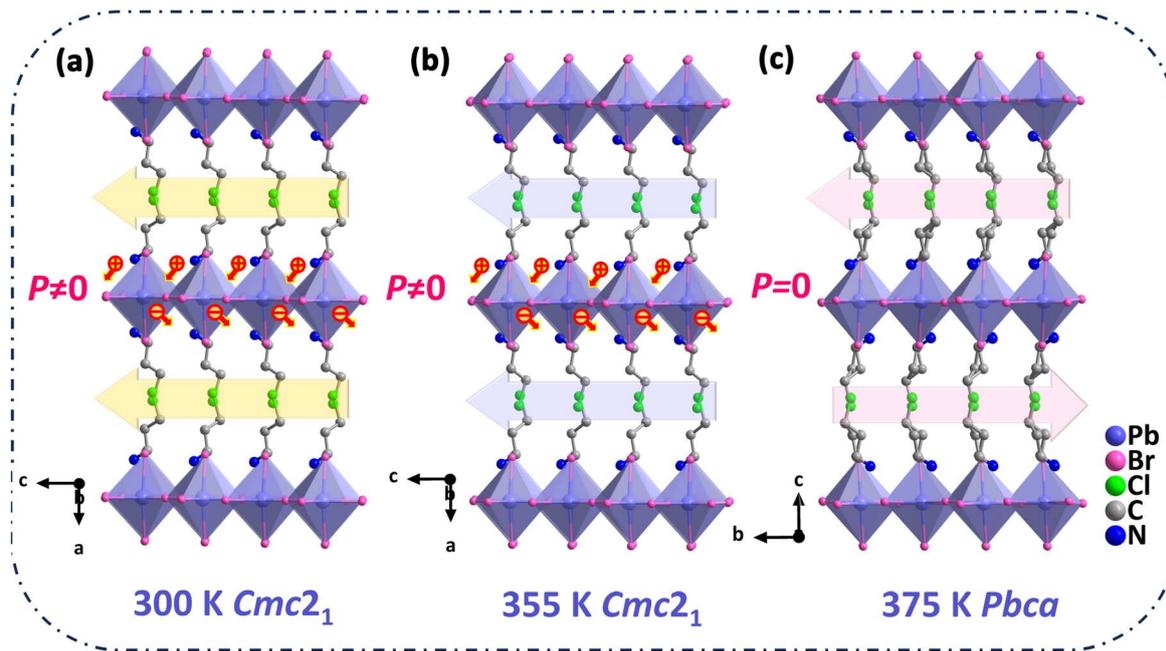
Fig. 3 Structural changes of (Cl-PA)$_2$PbBr$_4$ at (a) RTP, (b) ITP and (c) HTP.

we also obtained the structure of (Cl-PA)$_2$PbBr$_4$ at different temperatures through variable-temperature single-crystal X-ray diffraction (SCXRD). At room temperature (300 K), (Cl-PA)$_2$-PbBr$_4$ shows a polar structure with $Cmc2_1$ space group, which belongs to one of 10 polar point groups ($mm2$), and we mark it as the room temperature phase (RTP) (Fig. 3a). When the temperature is raised to 355 K (Fig. 3b), the crystal structure of (Cl-PA)$_2$PbBr$_4$ remains in the polar $Cmc2_1$ space group, and we label this state as the intermediate temperature phase (ITP). From Fig. 3a and b, it can be seen that Cl-PA$^+$ cations are in an ordered state below 365 K. Upon further heating to 375 K, the structure of (Cl-PA)$_2$PbBr$_4$ changes to the centrosymmetric orthorhombic space group of $Pbca$ (Fig. 3c) and the Cl-PA$^+$ cations exhibit obvious disorder, and this is called the high temperature phase (HTP). For the treatment of high-temperature crystal structures of (Cl-PA)$_2$PbBr$_4$, we adopted the same method as other similar perovskites.[9,30,31] The other crystallographic data of (Cl-PA)$_2$PbBr$_4$ at different temperatures are all listed in Tables S1–S8. We know that in molecular ferroelectrics, the high-temperature disorder and low-temperature order transition of organic units are crucial for the generation and regulation of ferroelectricity.[32–34] At HTP, Cl-PA$^+$ cations are in a dynamic disordered state due to thermal motion, resulting in a highly symmetrical structure of (Cl-PA)$_2$PbBr$_4$ and the random arrangement of local dipoles prevents the formation of macroscopic polarization. When the temperature drops below the Curie temperature (T_c = 365 K), the thermal motion of Cl-PA$^+$ cations is suppressed, and the orientation or position tends towards long-range ordered arrangement. This orderliness breaks the original symmetry (such as changing from centrosymmetry to polar space group) and induces the generation of spontaneous polarization. The symmetry breaking in (Cl-

PA)$_2$PbBr$_4$ conforms to Aizu notation of $mmmFmm2$, which satisfies the requirements of 88 species ferroelectric-type phase transition.[35]

Furthermore, by measuring the variation of the second-harmonic generation (SHG) signal with temperature, we can also detect the process of symmetry breaking in (Cl-PA)$_2$PbBr$_4$. At temperatures above 365 K, (Cl-PA)$_2$PbBr$_4$ is in the centrosymmetric phase, and the SHG signal should approach zero, which indicates the SHG-OFF state. When the temperature drops below T_c, the material undergoes symmetry breaking and transforms to a polar space group, resulting in a significant enhancement of the SHG signal, which indicates the SHG-ON state (Fig. 2b). We also compared the SHG intensity of (Cl-PA)$_2$PbBr$_4$ and KDP (KH$_2$PO$_4$) at the same particle size, and the results showed that the SHG intensity of (Cl-PA)$_2$PbBr$_4$ was 0.55 times that of KDP (Fig. S3), which is comparable to that of other hybrid perovskites ferroelectrics, such as [CH$_3$(CH$_2$)$_3$NH$_3$]$_2$(-CH$_3$NH$_3$)Pb$_2$Br$_7$ (0.4 × KDP),[36] (C$_4$H$_9$NH$_3$)$_2$CsPb$_2$Br$_7$ (0.5 × KDP)[37] and [(CH$_3$)$_3$NCH$_2$I]PbI$_3$ (0.65 × KDP).[38] Dielectric anomaly is a common characteristic of ferroelectric phase transitions. Near the T_c of ferroelectric materials, the dielectric constant reaches its peak and exhibits significant dielectric anomalies. Dielectric measurements of (Cl-PA)$_2$PbBr$_4$ (Fig. 2c) showed changes in the dielectric constant near 348 K and 365 K, which is consistent with the results of variable-temperature SCXRD testing and DSC testing. The observation of thermal hysteresis in both heating and cooling processes suggests that these phase transitions are first-order transitions.[5] Through the above structural analysis and the characterization of related physical properties, (Cl-PA)$_2$PbBr$_4$ has already met the conditions of polar structure, reversible polarization path, and dynamic phase transition ability, thus proving that it is

a potential ferroelectric. The ferroelectric hysteresis loop is the core experimental curve that characterizes its ferroelectricity, reflecting the nonlinear relationship between polarization intensity (P) and external electric field (E). Here, we measured the P–E hysteresis loops of (Cl-PA)$_2$PbBr$_4$ along the polar c-axis direction of crystal samples at different temperatures. As shown in Fig. 2d, the rectangular P–E hysteresis loops of (Cl-PA)$_2$PbBr$_4$ collected at 330 K afford the P_s values of ~1.3 μC cm^{-2}, which decreased with increasing temperature, consistent with the transition from the ferroelectric phase to paraelectric phase.

To gain insights into the ferroelectricity of (Cl-PA)$_2$PbBr$_4$, we compared and analyzed the non-covalent interactions in the structure of (PA)$_2$PbBr$_4$ and (Cl-PA)$_2$PbBr$_4$. After the Cl atom replaces the H atom on PA, the Cl-PA has a relatively large dipole moment ($\mu_{Cl\text{-}PA}$ = 3.3 D), which is a favorable factor for constructing molecular ferroelectrics. This is because the larger the dipole moment of the molecule, the more significant the charge separation within the molecule, and it will provide a stronger microscopic contribution for macroscopic polarization. Although organic amines have large dipole moments that are advantageous for constructing molecular ferroelectrics, it is still necessary to combine appropriate crystal structure design to enable these dipole moments to be arranged in an orderly manner. It is of great significance that precisely controlling the arrangement of organic amine molecules through non-covalent interactions is the core strategy for designing high-performance molecular ferroelectrics. In the crystal structure, the synergy and competition of weak interactions such as hydrogen bonding, VDW interactions, and halogen–halogen bonds can endow materials with dynamic response, structural flexibility, and functional tunability.

Hirshfeld surface analysis transforms the complex molecular interactions into visual and quantifiable data, providing a unique perspective for the study of non-covalent interactions.[39–41] The Hirshfeld surface and related 2D fingerprint plot were obtained based on CIF files through the CrystalExplorer program. Fig. S4a and S5a are the Hirshfeld surface of PA$^+$ and Cl-PA$^+$ cations and the intensive red spots indicate relatively strong interactions (the distance smaller than VDW distance), the blue regions correspond to long contacts (the distance exceeds VDW distance), the white regions correspond to the distance of contacts almost equal to VDW distance.[39] Hirshfeld surface and 2D fingerprint analyses reveal that the proportion of H–Br interactions in (PA)$_2$PbBr$_4$ and (Cl-PA)$_2$PbBr$_4$ is 43.1% (Fig. S4b) and 35.7% (Fig. S5b), respectively. Especially, the N–H⋯Br and C–H⋯Br hydrogen bonds in the structure are significantly weakened after halogen substitution (Fig. S6, N–H⋯Br for (PA)$_2$PbBr$_4$ is 52.3% and for (Cl-PA)$_2$PbBr$_4$ it is 48.4%, Fig. S7, C–H⋯Br for (PA)$_2$PbBr$_4$ is 17.5% and for (Cl-PA)$_2$PbBr$_4$ it is 14.3%), indicating that the interaction between the inorganic skeleton and the interlayer organic amine cations in (Cl-PA)$_2$-PbBr$_4$ is relatively weak, which gives the Cl-PA$^+$ cation a higher degree of freedom of movement. The strength of hydrogen bonds between interlayer cations and inorganic layers in (PA)$_2$PbBr$_4$ and (Cl-PA)$_2$PbBr$_4$ can also be confirmed from the crystal structure in Fig. 4a–d. The penetration depth of Cl-PA$^+$ cations (0.476 Å) in the adjacent inorganic layer is smaller than

that of PA$^+$ cations (0.511 Å), which demonstrated the PA$^+$ cations submerge deeper into the inorganic layer in (PA)$_2$PbBr$_4$. Therefore, PA$^+$ cations are closer to Br in the inorganic layer, forming shorter hydrogen bonds (Fig. 4b) and narrower interlayer space (6.574 Å, Fig. 4a). For N–H⋯Br hydrogen bonds, the shortest H–Br distance in (PA)$_2$PbBr$_4$ is 2.521 Å, corresponding to a ∠N–H⋯Br angle of 170.8°, while the shortest H–Br distance in (Cl-PA)$_2$PbBr$_4$ is 2.575 Å, corresponding to a ∠N–H⋯Br angle of 160.3° (Fig. S8). The strong N–H⋯Br hydrogen bonds in (PA)$_2$PbBr$_4$ may limit the vibrational degrees of freedom of PA$^+$ cations, leading to a weakened structural dynamic response of the material under temperature changes, which also explains why (PA)$_2$PbBr$_4$ did not undergo phase transition during temperature changes. In addition, the strong hydrogen bonds in (PA)$_2$PbBr$_4$ may limit the vibration or distortion of octahedra in the inorganic layer, stabilizing the structure in a more symmetrical state. That's because hydrogen bonding enhances the interaction between the organic and inorganic layers, strengthens interlayer coupling, makes the structure of the inorganic layer more stable, and limits the distortion of octahedra. The degree of distortion of PbBr$_6$ octahedra (Δd) in (PA)$_2$PbBr$_4$ (2.40×10^{-6}) is smaller than that of (Cl-PA)$_2$PbBr$_4$ (1.36×10^{-4}), indicating the rigid structure in (PA)$_2$PbBr$_4$. The specific calculation formula of Δd is as follows:[42]

$$\Delta d = \left(\frac{1}{6}\right) \sum \left[\frac{d_n - d}{d}\right]^2 \qquad (1)$$

where d is the mean Pb–Br bond length and d_n are the six individual Pb–Br bond lengths. We also evaluated the degree of structural distortion, including bond-angle variance (σ^2) and distortion index (D) of (PA)$_2$PbBr$_4$ and (Cl-PA)$_2$PbBr$_4$ using VESTA software in Table S8. Overall, the relatively rigid structure and limited cationic degrees of freedom make (PA)$_2$PbBr$_4$ less prone to structural phase transitions. After the introduction of the Cl-PA$^+$ cation with a larger dipole moment into the structure, the weakening of N–H⋯Br hydrogen bonding (Fig. 4d) gives the Cl-PA$^+$ cation a higher degree of freedom of movement, and more importantly, the additional halogen–halogen interaction (Fig. S5d and S5e) assists in the ordered arrangement of dipoles. Larger halogen atoms (Br) can form specific arrangements that affect the stacking and polar ordering of organic molecules. The Cl–Br distances (3.596 Å) between the organic cations and Pb–Br inorganic layer are less than the sum of van der Waals radii, and the ∠C–Cl⋯Br (172.4°) angle is greater than 170°, fully proving the existence of Cl–Br interactions in the RTP of (Cl-PA)$_2$PbBr$_4$ (Fig. S9a).[43] As the temperature increases, the Cl⋯Br interactions in ITP and the HTP gradually weaken (Fig. S9b and S9c). The Cl⋯Br interactions are consistent with Type-I halogen bond criteria.[43] The larger dynamic freedom degrees of Cl-PA$^+$ cations and the higher degree of distortion of PbBr$_6$ octahedra make (Cl-PA)$_2$-PbBr$_4$ more prone to phase transition during temperature changes. Fig. 4e and f contain the percentages of contributions of different contacts in (PA)$_2$PbBr$_4$ and (Cl-PA)$_2$PbBr$_4$, which is based on the organic cation. We can intuitively see that
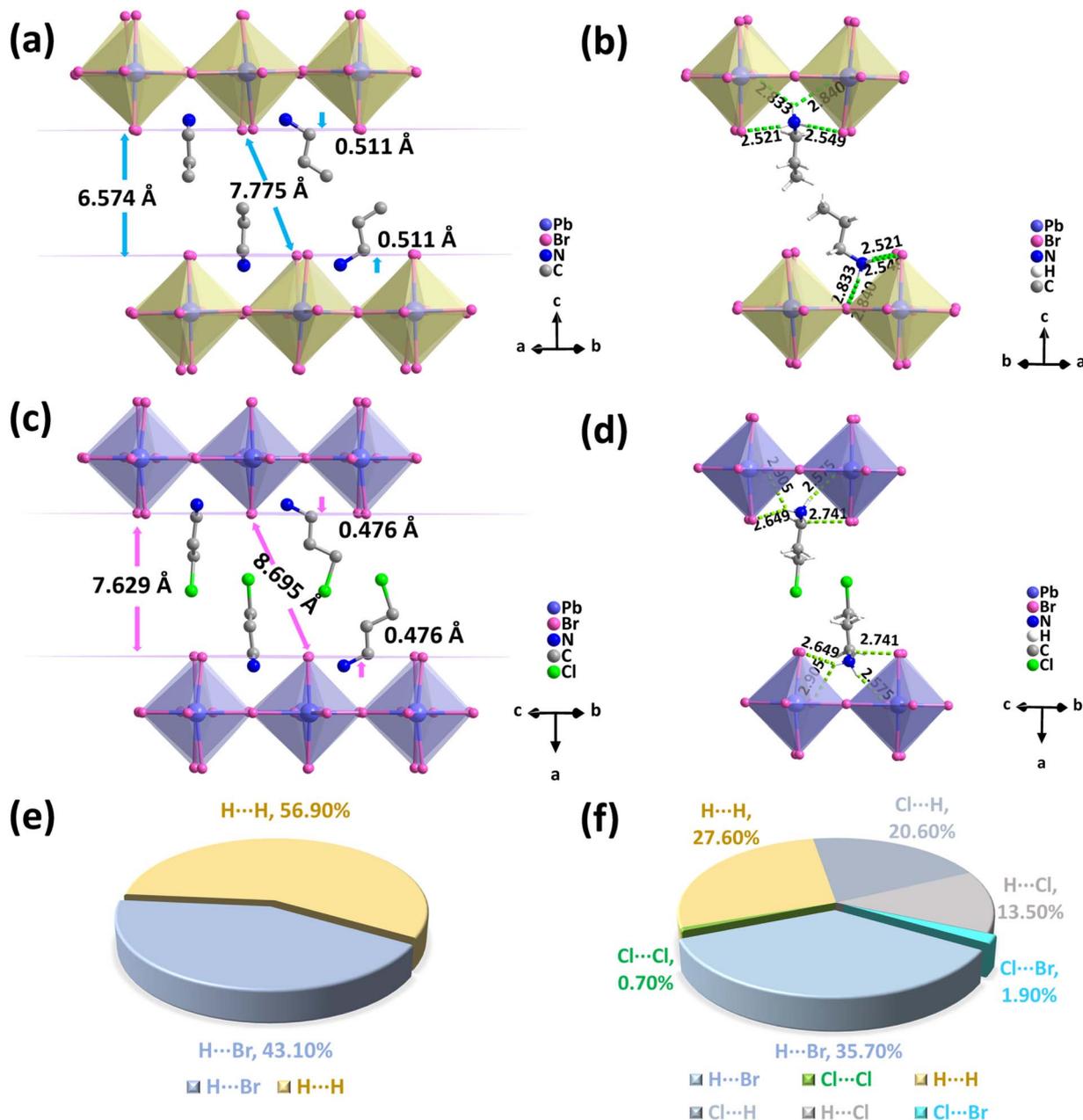
Fig. 4 The interlayer spacing, Br–Br distance between adjacent inorganic layers and the penetration depth of organic cations in $(PA)_2PbBr_4$ (a) and $(Cl-PA)_2PbBr_4$ (c). The H–Br distance in $(PA)_2PbBr_4$ (b) and $(Cl-PA)_2PbBr_4$ (d). The percentages of contributions of different contacts in the crystal structure of $(PA)_2PbBr_4$ (e) and $(Cl-PA)_2PbBr_4$ (f) based on organic cations.

introducing halogenated amines between adjacent inorganic layers can regulate non-covalent interactions in the structure, and this slight regulation induces the ferroelectricity of $(Cl-PA)_2PbBr_4$. Specifically, the regulation of the hydrogen bond network increases the freedom of movement of organic cations, facilitating the occurrence of ferroelectric phase transition. At the same time, the direction of dipoles is fixed by halogen–halogen interactions, inducing directional rearrangements of dipoles. These two non-covalent interactions work together to construct the ferroelectric $(Cl-PA)_2PbBr_4$. In addition to conducting Hirshfeld surface analysis on organic cations, we also

conducted Hirshfeld surface analysis on anionic frameworks. We individually selected a unit in the inorganic layer to analyze how the inorganic layer is surrounded by organic amine cations. Hirshfeld surface analysis of the inorganic octahedron in $(PA)_2PbBr_4$ will clearly reveal a complex non-covalent interaction network dominated by hydrogen bonds, supplemented by a large number of VDW forces (Fig. S10). In $(Cl-PA)_2PbBr_4$, in addition to hydrogen bonding, halogen–halogen interactions between inorganic frameworks, and VDW forces, halogen–halogen interactions (Br···Cl) between organic amine cations and inorganic frameworks were also introduced (Fig. S11). The

results of Hirshfeld surface analysis based on an inorganic skeleton (Fig. S12) indicate that the proportion of Br···H interactions in $(PA)_2PbBr_4$ is 90.20%, while in $(Cl-PA)_2PbBr_4$, the proportion of Br···H interactions is 87.00%. This indicates that the Br···H interactions are stronger in the structure of $(PA)_2$-$PbBr_4$. The Br···H interactions mainly refer to the N–H···Br and C–H···Br interactions between the octahedral cations and the organic cations. This finding is consistent with the conclusions drawn from the Hirshfeld surface analysis based on the organic cations. In addition, it can also be confirmed that there is Br···Cl interaction between the inorganic skeleton and the organic amine cation in $(Cl-PA)_2PbBr_4$. Therefore, in both $(PA)_2PbBr_4$ and $(Cl-PA)_2PbBr_4$, Hirshfeld surface analysis was performed on the organic cation and inorganic anionic frameworks, respectively, and the conclusions were consistent.

We know that non-covalent interactions are extremely temperature sensitive. In $(Cl-PA)_2PbBr_4$, there are fundamental differences in the non-covalent interactions between the RTP (ferroelectric phase) and the HTP (paraelectric phase), which are the driving forces behind ferroelectric phase transitions and spontaneous polarization. In the ferroelectric phase, the system is in an ordered state with the lowest energy. All non-covalent interactions reach their optimal and most stable configurations, and work together to stabilize the ferroelectric state. Moreover, halogen bonds and hydrogen bonds work together to determine the tilt direction and angle of organic cations. The halogen bond acts as a "lock buckle" that holds the other end of the organic cation in place, thereby "tightening" the entire cation together with the hydrogen bond, directing it in a specific direction and generating a net dipole moment. The most prominent feature of the ferroelectric phase is that hydrogen bonds and halogen bonds are no longer independent, but synergistically control the orientation, tilt angle, and position of organic cations, thereby stabilizing polar structures with net dipole moments (Fig. S13a, b and S14a). When the temperature rises and the thermal energy gradually exceeds the energy scale of these non-covalent interactions, the system undergoes a phase transition and enters the disordered paraelectric phase. In the HTP, all non-covalent interactions are dominated by thermal motion. Organic cations undergo rapid disordered motion (rotation and oscillation, Fig. S13c and S14b). Among them, N and H atoms will experience severe orientational disorder, while C atoms will experience conformational disorder. In addition, it can be seen from the significantly increased atomic displacement parameter of halogen atoms that their position in space is very uncertain (Table S9). That is, at high temperatures, halogen atoms are not "stationary in a vague position", but "rapidly moving between multiple possible positions". Therefore, the hydrogen bonds and halogen bonds become very weak or only exist instantaneously, which undoubtedly exacerbates the overall disordered movement of cations (Fig. S14b). In summary, the dynamic disorder of hydrogen bonds from low temperature to high temperature and the "formation breakage" process of halogen bonds from low temperature to high temperature are one of the core mechanisms driving the ferroelectric paraelectric phase transition of $(Cl-PA)_2PbBr_4$. Moreover, the hydrogen-bond

parameters of $(PA)_2PbBr_4$ and $(Cl-PA)_2PbBr_4$ at different temperatures are listed in Tables S10–S13. Meanwhile, as halogen bonds can enhance the long-range ordering of local dipoles and improve macroscopic polarizability by fixing the relative orientation of organic components, this is positively correlated with the piezoelectric coefficient d_{33}. Therefore, the relatively large d_{33} of $(Cl-PA)_2PbBr_4$ (36 pC/N, Fig. S15) may be related to halogen–halogen interactions, as halogen–halogen interactions can induce non-centrosymmetric structures and dipole ordering to enhance piezoelectric activity.[44] The comparison of d_{33} values between $(Cl-PA)_2PbBr_4$ and other hybrid perovskites is shown in Fig. S16.

Based on the semiconductor properties of $(Cl-PA)_2PbBr_4$, a stable built-in electric field formed by the spontaneous polarization of the ferroelectric phase can automatically separate electron–hole pairs generated by X-ray excitation, significantly reducing recombination losses. Compared to traditional X-ray detectors that require high voltage to drive carrier migration, this significantly simplifies the structure of the device and reduces energy consumption. Next, the X-ray detection performance of the $(Cl-PA)_2PbBr_4$ single crystal was systematically investigated. Fig. 5a shows the absorption coefficients as a function of X-ray photon energy of typical detector materials. The absorption coefficient of $(Cl-PA)_2PbBr_4$ is comparable to that of α-Se due to the high-Z element. The X-ray detectors were assembled with a typical photoconductor structure of Au/$(Cl-PA)_2PbBr_4$/Au. The mobility-lifetime $(\mu\tau)$ value is the "performance lever" of X-ray detector materials, which is directly related to the core indicators of the detector.[45–47] As fitted in Fig. 5b, the $(Cl-PA)_2PbBr_4$ single crystal has a $\mu\tau$ product of 1.32×10^{-3} cm^2 V^{-1}, which is superior to that of other 2D hybrid perovskites previously reported, such as $PA_2MHy_2Pb_3$-Br_{10} (MHy is methylhydrazine, 4.72×10^{-4} cm^2 V^{-1})[48] and $(2IPA)_2FAPb_2I_7$ (2IPA = 2-iodopropylammonium, FA is formamidinium, 1.2×10^{-3} cm^2 V^{-1}).[49] The ratio of the photovoltaic voltage generated by ferroelectrics through the bulk photovoltaic effect to the incident light intensity reflects the intrinsic efficiency of the material in converting light energy into electrical energy. A larger photovoltaic voltage will generate a strong built-in electric field, which enhances the ability of carrier directional migration. As shown in Fig. 5c, the bulk photovoltaics of $(Cl-PA)_2PbBr_4$ through current–voltage $(I–V)$ traces under X-ray are estimated to be 1.40 V, which is beneficial for achieving passive X-ray detection. Furthermore, the photocurrent density in Fig. 5d–g and S17 exhibits a good linear relationship with the X-ray dose rate under different biases. The sensitivity increases with the increase of the bias and even under 0 V bias the sensitivity of the device can also reach 127.2 μC Gy^{-1} cm^{-2} (Fig. 5g), which is much better than that of the device based on the (isopropylammonium)$_2PbBr_4$ ferroelectric (51.4 μC Gy^{-1} cm^{-2} at 0 V bias).[50] The Limit of Detection (LoD) of an X-ray detector refers to the minimum X-ray dose or photon flux that the detector can reliably identify, usually based on the signal strength corresponding to a Signal to Noise Ratio (SNR) of ≥ 3. The LoD of 52 nGy s^{-1} is derived from the linear fitting with an SNR of 3 shown in Fig. 5h, which is lower than that of some hybrid perovskite-based X-ray detectors under 0 V bias
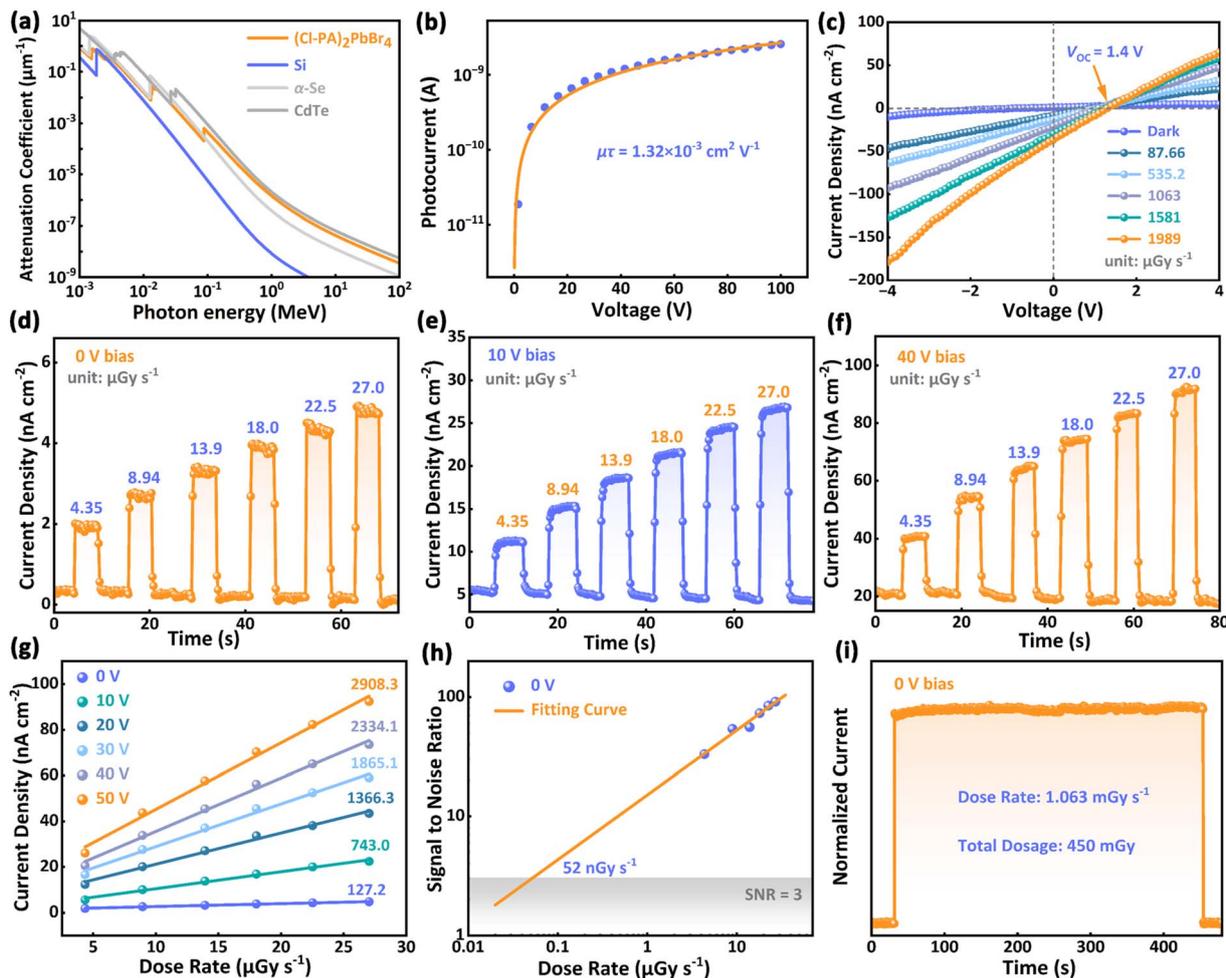
Fig. 5 (a) Comparison of the X-ray absorption coefficients of (Cl-PA)$_2$PbBr$_4$ with commercial Si, α-Se, and CdTe. (b) Response current under X-ray irradiation and fitting curves of (Cl-PA)$_2$PbBr$_4$. (c) I–V curves of the (Cl-PA)$_2$PbBr$_4$ device in the dark and under different dose rates of X-ray irradiation. Time-dependent current response of the (Cl-PA)$_2$PbBr$_4$ single crystal device under different dose rates of X-ray irradiation at 0 V (d), 10 V (e) and 40 V (f) bias. (g) Photocurrent density as a function of X-ray dose rate at different biases. (h) SNR of the (Cl-PA)$_2$PbBr$_4$ device under different dose rates of X-rays at 0 V bias. (i) The stability of the (Cl-PA)$_2$PbBr$_4$ detector under continuous X-ray irradiation at 0 V bias.

(Table S14) and is far lower than the dose rate of a regular X-ray medical imaging (5.5 μGy s^{-1}). The photostability of the device is crucial due to the phase transition, ion migration, or interface reaction induced by light waves. We measured the photostability of single crystal devices based on (Cl-PA)$_2$PbBr$_4$ under long-term X-ray detection. In Fig. 5i, the photocurrent exhibits no significant changes after passing through a total amount of 450 mGy X-ray dosage, demonstrating its high radiation stability. These photoelectric test results indicate that the excellent semiconductor properties and unique bulk photovoltaic effect make (Cl-PA)$_2$PbBr$_4$ highly promising for passive X-ray detection.

Conclusions

In conclusion, non-covalent interactions provide structural flexibility and dynamism for constructing molecular ferroelectrics, enabling specific arrangements of molecules and facilitating polarization generation and reversal. Obviously,

balancing different non-covalent interactions is a design challenge. We modified the interlayer organic cations through a halogenation strategy to regulate non-covalent interactions in the structure. The introduction of Cl-PA$^+$ affects the hydrogen bonding network between the inorganic layer and organic cations, enhances the dynamic degree of freedom of Cl-PA$^+$ cations, and makes (Cl-PA)$_2$PbBr$_4$ prone to phase transition. More importantly, the additional halogen–halogen interactions and hydrogen bonding in the structure collaboratively result in molecular directional rearrangement, which regulates crystal symmetry and achieves polarization reversal. In addition, non-covalent interactions are extremely temperature sensitive. The dynamic disorder of hydrogen bonds from low to high temperatures, as well as the formation and breaking of halogen bonds, are important factors driving the ferroelectricity of (Cl-PA)$_2$PbBr$_4$. Finally, the photoferroelectric semiconductor (Cl-PA)$_2$PbBr$_4$ with high T_c (365 K) and a large piezoelectric coefficient (d_{33} = 36 pC/N) has also demonstrated excellent performance in the field of passive X-ray detection.

Author contributions

Y. He prepared the samples and conducted relevant physical property tests. S. Wu and X. Li tested the photoelectric properties. Q. Wang, R. Zhao and L. Pan contributed to the organization of the supporting information. C. Qin helped with the relevant optical testing. X. Zhang provided suggestions for the article. D. Fu designed, directed and wrote the article. All the authors discussed and commented on the article.

Conflicts of interest

There are no conflicts to declare.

Data availability

CCDC 2405625–2405627 (2405625 for the crystal structure of $(Cl-PA)_2PbBr_4$ at 300 K, 2405626 for the crystal structure of $(Cl-PA)_2PbBr_4$ at 355 K and 2405627 for the crystal structure of $(Cl-PA)_2PbBr_4$ at 375 K) contain the supplementary crystallographic data for this paper.[51a–c]

Supplementary information: structural information, PXRD patterns, synthesis process of $(Cl-PA)_2PbBr_4$, Hirshfeld surface and related 2D fingerprint plot and additional information (PDF). See DOI: https://doi.org/10.1039/d5sc05946a.

Acknowledgements

Notes and references

1 H.-Y. Ye, Y.-Y. Tang, P.-F. Li, W.-Q. Liao, J.-X. Gao, X.-N. Hua, H. Cai, P.-P. Shi, Y.-M. You and R.-G. Xiong, *Science*, 2018, **361**, 151–155.

2 D.-W. Fu, H.-L. Cai, Y. Liu, Q. Ye, W. Zhang, Y. Zhang, X.-Y. Chen, G. Giovannetti, M. Capone, J. Li and R.-G. Xiong, *Science*, 2013, **339**, 425–428.

3 H.-Y. Zhang, Y.-Y. Tang, Z.-X. Gu, P. Wang, X.-G. Chen, H.-P. Lv, P.-F. Li, Q. Jiang, N. Gu, S. Ren and R.-G. Xiong, *Science*, 2024, **383**, 1492–1498.

4 X. Cao, S. Ding, G. Du, Z. Jing, Y. Xiong, Z. Feng, H. Ji, Q. Pan and Y. You, *Adv. Mater.*, 2025, **37**, 2416837.

5 H.-Y. Liu, H.-Y. Zhang, X.-G. Chen and R.-G. Xiong, *J. Am. Chem. Soc.*, 2020, **142**, 15205–15218.

6 W.-F. Deng, Y.-X. Li, Y.-X. Zhao, J.-S. Hu, Z.-S. Yao and J. Tao, *J. Am. Chem. Soc.*, 2023, **145**, 5545–5552.

7 Y. Ma, W. Li, Y. Liu, W. Guo, H. Xu, L. Tang, Q. Fan, H. Rong, J. Luo and Z. Sun, *Angew. Chem., Int. Ed.*, 2025, **64**, e202424279.

8 S. Han, M. Li, Y. Liu, W. Guo, M.-C. Hong, Z. Sun and J. Luo, *Nat. Commun.*, 2021, **12**, 284.

9 M. Mączka, J. K. Zaręba, A. Gągor, K. Fedoruk-Piskorska, D. Stefańska, D. Drozdowski, M. Ptak and A. Sieradzki, *ACS Appl. Mater. Interfaces*, 2024, **16**, 60564–60575.

10 M. A. Cassingham, Y. G. Goh, E. T. McClure, T. L. Hodgkins, W. G. Zhang, M. L. Liang, J. M. Dawlaty, P. I. Djurovich, R. Haiges, P. S. Halasyamani, C. N. Savory, M. E. Thompson and B. C. Melot, *ACS Appl. Mater. Interfaces*, 2023, **15**, 18006–18011.

11 P.-P. Shi, Y.-Y. Tang, P.-F. Li, W.-Q. Liao, Z.-X. Wang, Q. Ye and R.-G. Xiong, *Chem. Soc. Rev.*, 2016, **45**, 3811–3827.

12 K. Kim, Y. Li and K. M. Ok, *J. Am. Chem. Soc.*, 2025, **147**, 2880–2888.

13 C.-K. Yang, W.-N. Chen, Y.-T. Ding, J. Wang, Y. Rao, W.-Q. Liao, Y. Xie, W. Zou and R.-G. Xiong, *J. Am. Chem. Soc.*, 2019, **141**, 1781–1787.

14 J. Lasave, J. Kohanoff, R. L. Migoni and S. Koval, *Physica B*, 2009, **404**, 2736–2738.

15 H. S. Choi, S. Li, I.-H. Park, W. H. Liew, Z. Zhu, K. C. Kwon, L. Wang, I.-H. Oh, S. Zheng, C. Su, Q.-H. Xu, K. Yao, F. Pan and K. P. Loh, *Nat. Commun.*, 2022, **13**, 794.

16 M. C. Storer and C. A. Hunter, *Chem. Soc. Rev.*, 2022, **51**, 10064–10082.

17 A. S. Tayi, A. Kaeser, M. Matsumoto, T. Aida and S. I. Stupp, *Nat. Chem.*, 2015, **7**, 281–294.

18 D. Fu, Y. Zhang, Z. Chen, L. Pan, Y. He and J. Luo, *Small*, 2024, **20**, 2403198.

19 J. Xue, Y. Huang, Y. Liu, Z. Chen, H. H. -Y. Sung, I. D. Williams, Z. Zhu, L. Mao, X. Chen and H. Lu, *Angew. Chem., Int. Ed.*, 2023, **62**, e202304486.

20 T. Schmitt, S. Bourelle, N. Tye, G. Soavi, A. D. Bond, S. Feldmann, B. Traore, C. Katan, J. Even, S. E. Dutton and F. Deschler, *J. Am. Chem. Soc.*, 2020, **142**, 5060–5067.

21 R. Chakraborty, P. K. Rajput, G. M. Anilkumar, S. Maqbool, R. Das, A. Rahman, P. Mandal and A. Nag, *J. Am. Chem. Soc.*, 2023, **145**, 1378–1388.

22 K. T. Mahmudov, M. N. Kopylovich, M. F. C. Guedes Da Silva and A. J. L. Pombeiro, *Coord. Chem. Rev.*, 2017, **345**, 54–72.

23 H.-Y. Zhang, Z.-X. Zhang, X.-J. Song, X.-G. Chen and R.-G. Xiong, *J. Am. Chem. Soc.*, 2020, **142**, 20208–20215.

24 Q.-Q. Jia, G. Teri, J.-Q. Luo, H.-F. Ni, P.-Z. Huang, M.-M. Lun, Z.-X. Zhang, Y. Zhang and D.-W. Fu, *J. Am. Chem. Soc.*, 2024, **146**, 21120–21128.

25 Y. Ai, R. Sun, W. Liao, X. Song, Y. Tang, B. Wang, Z. Wang, S. Gao and R. Xiong, *Angew. Chem., Int. Ed.*, 2022, **61**, e202206034.

26 H. Nishikawa, Y. Okumura, D. Kwaria, A. Nihonyanagi and F. Araoka, *Adv. Mater.*, 2025, 2501946.

27 K. Du, Q. Tu, X. Zhang, Q. Han, J. Liu, S. Zauscher and D. B. Mitzi, *Inorg. Chem.*, 2017, **56**, 9291–9302.

28 C. Zhang, H. Xiao, Q. Guan, T. Zhu, L. Liang, R. Li, H. Ye, X. Niu and J. Luo, *J. Mater. Chem. C*, 2023, **11**, 5116–5122.

29 J. A. McNulty and P. Lightfoot, *IUCrJ*, 2021, **8**, 485–513.

30 M. Mączka, J. Kudrawiec, K. Fedoruk-Piskorska, D. Stefańska, A. Gągor, M. Drozd, S. Smółka and A. Sieradzki, *Inorg. Chem.*, 2025, **64**, 4501–4513.

31 M. Ptak, B. Dziuk, S. Smółka, J. Osmólska, M. Stefanski, A. Łukowiak and A. Sieradzki, *J. Phys. Chem. C*, 2023, **127**, 22204–22211.

32 K. Li, Z.-G. Li, J. Xu, Y. Qin, W. Li, A. Stroppa, K. T. Butler, C. J. Howard, M. T. Dove, A. K. Cheetham and X.-H. Bu, *J. Am. Chem. Soc.*, 2022, **144**, 816–823.

33 H.-Y. Zhang, Y.-Y. Tang, P.-P. Shi and R.-G. Xiong, *Acc. Chem. Res.*, 2019, **52**, 1928–1938.

34 Q. Pan, Z.-X. Gu, R.-J. Zhou, Z.-J. Feng, Y.-A. Xiong, T.-T. Sha, Y.-M. You and R.-G. Xiong, *Chem. Soc. Rev.*, 2024, **53**, 5781–5861.

35 K. Aizu, *J. Phys. Soc. Jpn.*, 1969, **27**, 387–396.

36 L. Li, X. Liu, Y. Li, Z. Xu, Z. Wu, S. Han, K. Tao, M. Hong, J. Luo and Z. Sun, *J. Am. Chem. Soc.*, 2019, **141**, 2623–2629.

37 Z. Wu, C. Ji, L. Li, J. Kong, Z. Sun, S. Zhao, S. Wang, M. Hong and J. Luo, *Angew. Chem., Int. Ed.*, 2018, **57**, 8140–8143.

38 X.-N. Hua, W.-Q. Liao, Y.-Y. Tang, P.-F. Li, P.-P. Shi, D. Zhao and R.-G. Xiong, *J. Am. Chem. Soc.*, 2018, **140**, 12296–12302.

39 M. A. Spackman and D. Jayatilaka, *CrystEngComm*, 2009, **11**, 19–32.

40 S. L. Tan, M. M. Jotani and E. R. T. Tiekink, *Acta Cryst.*, 2019, **75**, 308–318.

41 M. A. Spackman and D. Jayatilaka, *CrystEngComm*, 2009, **11**, 19–32.

42 L. Mao, P. Guo, M. Kepenekian, I. Hadar, C. Katan, J. Even, R. D. Schaller, C. C. Stoumpos and M. G. Kanatzidis, *J. Am. Chem. Soc.*, 2018, **140**, 13078–13088.

43 G. Cavallo, P. Metrangolo, R. Milani, T. Pilati, A. Priimagi, G. Resnati and G. Terraneo, *Chem. Rev.*, 2016, **116**, 2478–2601.

44 W.-Q. Liao, D. Zhao, Y.-Y. Tang, Y. Zhang, P.-F. Li, P.-P. Shi, X.-G. Chen, Y.-M. You and R.-G. Xiong, *Science*, 2019, **363**, 1206–1210.

45 Y. Wang, M. Li, Z. Chai, Y. Wang and S. Wang, *Angew. Chem., Int. Ed.*, 2023, **62**, e202304638.

46 Y. Jiang, C. Zhang, Z. Zhu, J. Wu, P. Yu, Y. Zeng, H. Ye, H. Dai, R. Li, Q. Guan, G. Chen, H. Yang and J. Luo, *Angew. Chem., Int. Ed.*, 2024, **63**, e202407305.

47 D. Fu, Z. Chen, S. Wu, Y. Ma and X.-M. Zhang, *Chem. Mater.*, 2024, **36**, 5284–5292.

48 R. Li, B. Xu, J. Wu, S. You, C. Zhang, C. Ji, Z. Lin and J. Luo, *Adv. Funct. Mater.*, 2024, **34**, 2404353.

49 S. You, P. Yu, J. Wu, Z. Zhu, Q. Guan, L. Li, C. Ji, X. Liu and J. Luo, *Adv. Sci.*, 2023, **10**, 2301149.

50 Y. He, Z. Chen, D.-W. Fu, Z. Hou, X.-M. Zhang and D. Fu, *Chem. Mater.*, 2024, **36**, 994–1003.

51 (*a*) CCDC 2405625: Experimental Crystal Structure Determination, 2025, DOI: **10.5517/ccdc.csd.cc2lr7tf**; (*b*) CCDC 2405626: Experimental Crystal Structure Determination, 2025, DOI: **10.5517/ccdc.csd.cc2lr7vg**; (*c*) CCDC 2405627: Experimental Crystal Structure Determination, 2025, DOI: **10.5517/ccdc.csd.cc2lr7wh**.